nature sustainability

Article

https://doi.org/10.1038/s41893-026-01849-0

Energy-efficient electrified ethylene synthesis in CO-starved environment

Received: 22 August 2024

Accepted: 26 April 2026

Published online: 04 June 2026

Check for updates

Yuanjun Chen[1,2,3,6], Pengfei Ou[1,2,3,6], Xinyue Wang[1,6], Rui Kai Miao[4,6], Yuxin Chang[1], Adnan Ozden[4,5], Xiao-Yan Li[1,2,3], Jianan Erick Huang[1], Weiyan Ni[1,2,3], Roham Dorakhan[1], Jinqiang Zhang[1], Ke Xie[1,2,3], David Sinton[4] ✉ & Edward H. Sargent[1,2,3] ✉

Electrochemical synthesis using carbon monoxide (CO) has the potential to offer sustainable ethylene (C_2H_4) production. However, there is a trade-off between the energy efficiency and the single-pass carbon efficiency achieved in such systems, especially at the outlet of a high-single-pass-carbon-efficiency reaction environment where the system becomes starved of CO. Here we pursued catalysts that achieve efficient C–C coupling even at a low CO concentration near the outlet of a high-single-pass-carbon-efficiency reactor, by enhancing CO coverage on the catalyst surface to facilitate the deoxygenation of the key intermediate *CHCOH, and thereby steer the reaction towards ethylene. The use of a nitrogen- and phosphorous-co-doped carbon layer obtained simultaneously 38% ethylene energy efficiency and 73% single-pass carbon efficiency at 200 mA cm^{-2}. We estimate a total energy cost of C_2H_4 production of 141 GJ t^{-1}. When the CO is derived from CO_2 reduction and the CO_2 feedstock is obtained through direct air capture, and wind electricity is employed, the cradle-to-gate carbon intensity reaches −2.5 t CO_2e t^{-1} C_2H_4, much lower than a +2.2 t CO_2e t^{-1} carbon footprint of C_2H_4 synthesis based on naphtha cracking. This work provides a viable strategy to enable electrified ethylene production in a CO-starved environment.

The chemical sector accounts for 28% of total industrial energy demand[1]. Today this is met largely through the utilization of fossil fuels, and thus contributes substantially to CO_2 emissions[2]. Ethylene (C_2H_4), with a present-day production rate of 150 million tonnes per year globally, is the most-produced hydrocarbon chemical[3]. Scaled approaches to C_2H_4 production involve steam cracking of naphtha derived from crude oil, and ethane cracking[4,5] (Fig. 1a). The utilization of these feedstocks and associated emissions lead to an average of 2.2 tonnes of CO_2 equivalent per tonne of C_2H_4 produced[6]. Methane and other light hydrocarbons are produced as byproducts in these processes, and this increases both separation energy demands and CO_2 emissions when these are combusted[7]. This militates against full decarbonization of present-day C_2H_4 production routes and motivates alternative pathways towards substantial reductions in the carbon intensity of ethylene[8].

Electrosynthesis of C_2H_4 powered using low-carbon electricity provides a route to utilize CO_2 (such as that captured from the air) as feedstock[9–11] (Fig. 1b–c, Supplementary Table 1 and Supplementary Notes 1–5). The energy cost involved in the electrosynthesis of C_2H_4 is dominated by two factors: the electrolyser C_2H_4 energy efficiency (EE) and the energy required to separate C_2H_4 from the tailgas mixture that contains unreacted CO_2/CO as well as carbon-containing and H_2

[1]Department of Electrical and Computer Engineering, University of Toronto, Toronto, Ontario, Canada. [2]Department of Chemistry, Northwestern University, Evanston, IL, USA. [3]Department of Electrical and Computer Engineering, Northwestern University, Evanston, IL, USA. [4]Department of Mechanical and Industrial Engineering, University of Toronto, Toronto, Ontario, Canada. [5]Department of Mechanical and Nuclear Engineering, Khalifa University, Abu Dhabi, United Arab Emirates. [6]These authors contributed equally: Yuanjun Chen, Pengfei Ou, Xinyue Wang, Rui Kai Miao.
✉e-mail: sinton@mie.utoronto.ca; ted.sargent@utoronto.ca

https://doi.org/10.1038/s41893-026-01849-0

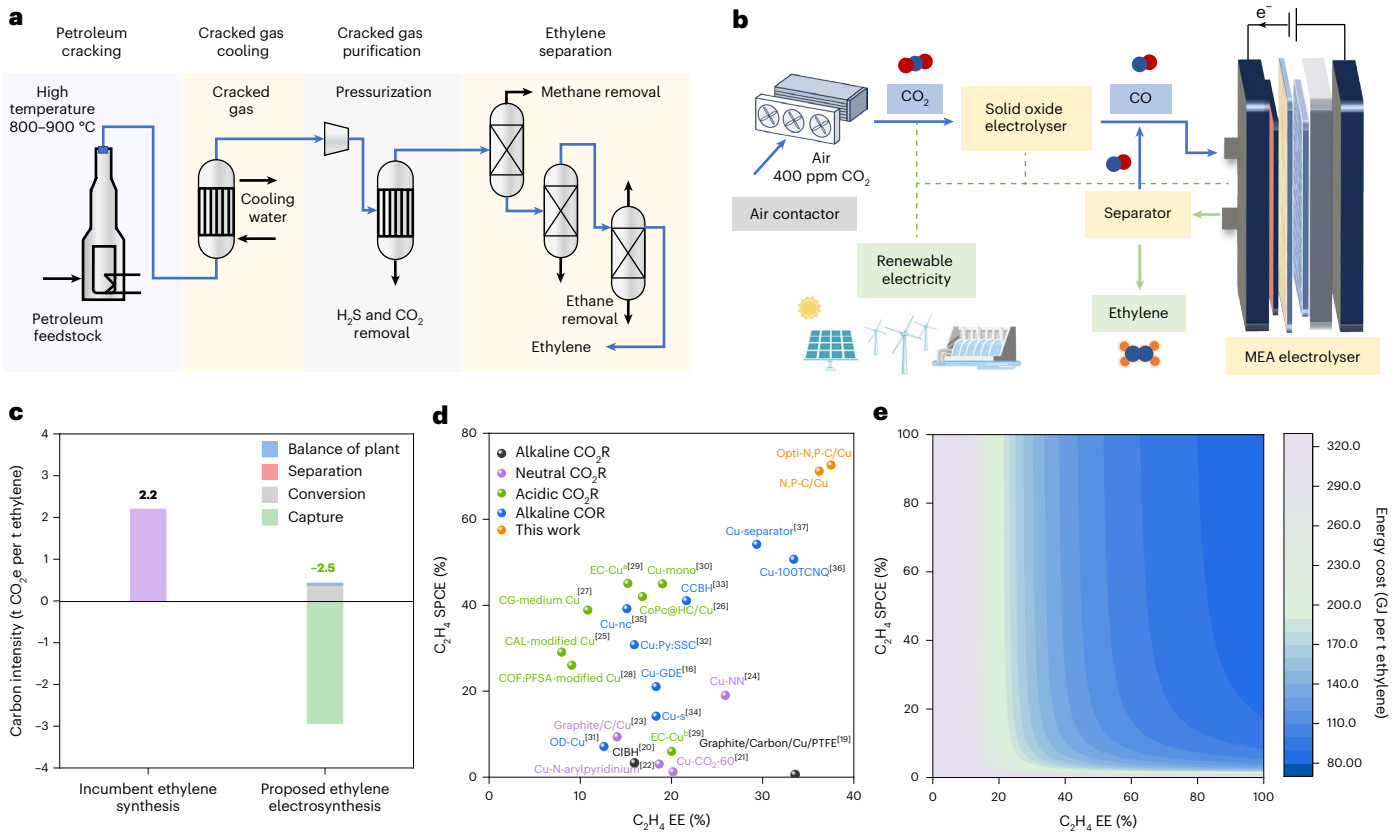

Fig. 1 | Synthesis of ethylene using low-carbon-intensity electricity. a, Existing thermochemical route to ethylene production. **b**, Electrochemical system for ethylene production. **c**, Life cycle assessment of the carbon intensity of ethylene production using existing routes versus an electrochemical system. Data for life cycle assessment calculation of the electrochemical system are from this work. **d**, The C_2H_4 EE and C_2H_4 SPCE performance assessment of the N,P-C/Cu electrode in this work and literature benchmark CO_2R and COR systems, including alkaline CO_2R, neutral CO_2R, acidic CO_2R and alkaline COR. **e**, Energy cost consumption for ethylene production associated with C_2H_4 EE and C_2H_4 SPCE.

side products[12–15]. The separation energy cost is minimized when the C_2H_4 volume fraction in the tailgas is maximized: this is achieved by maximizing the C_2H_4 single-pass conversion efficiency (SPCE) and the proportion of carbon-containing feedstock converted to the desired C_2H_4 product in a single traverse of the electrolyser[13,16], and by simultaneously minimizing the competing H_2 evolution reaction (HER) (Supplementary Note 6). A higher C_2H_4 volume fraction in the tailgas enables fewer separation stages, reduced compression duty, and equipment for gas-handling and separation that is smaller in size; this is the result of lowered volumetric flow per unit of C_2H_4 produced. It also enables more convenient storage and transport, meeting blending thresholds. These factors may enable decentralized deployments with limited utilities[17,18]. High C_2H_4 SPCE requires steering reaction selectivity towards C_2H_4 rather than other carbon-containing products, particularly under reactant-starved conditions at the outlet of a reactor operated at high SPCE. This demands that high selectivity be maintained even when the CO_2/CO reactant is substantially depleted in the final stages of the reaction chamber.

Recent advancements in C_2H_4 electrosynthesis, specifically via CO_2 electroreduction (CO_2R) in alkaline and neutral electrolytes, have achieved a C_2H_4 EE of 30% (refs. 19–24). However, the high EE comes at the expense of C_2H_4 SPCE, which typically remains below 25% due to the loss of at least 75% of CO_2 through its reaction with hydroxide, leading to carbonate- and bicarbonate-related losses of carbon atom efficiency[13,25] (Fig. 1d). Using acidic electrolytes shows promise in enhancing CO_2 utilization, as it enables local regeneration of CO_2 (refs. 25–30). In these systems, though, the challenge is to suppress the kinetically favourable HER. The most efficient earlier study of acidic CO_2R to C_2H_4 has demonstrated a C_2H_4 EE of 20% (ref. 30) (Fig. 1d). Using CO electroreduction (COR) overcomes the issue of CO_2 loss to (bi)carbonate[31–33]. Minimizing the all-in C_2H_4 production energy requires simultaneous achievement of high C_2H_4 EE and high C_2H_4 SPCE (Fig. 1e). Much progress has been made in producing C_2H_4 via COR[16,31–37] (Fig. 1d); we took the view that joint optimization of C_2H_4 EE and C_2H_4 SPCE would be of practical interest to the field and could simultaneously raise topics of research interest in catalyst and systems design. These considerations motivated us to develop C_2H_4 catalyst designs that would continue to work well even in a CO-starved reaction environment—a key challenge for simultaneously achieving high C_2H_4 EE and C_2H_4 SPCE.

We first identified a trade-off between C_2H_4 EE and C_2H_4 SPCE that limits energy-efficient electrified ethylene production. Pursuing a high C_2H_4 SPCE creates a CO-depleted environment at the catalyst surface due to reactant consumption resulting from high single-pass conversion, which leads to a decline in C_2H_4 EE. To overcome this trade-off, we sought a strategy that goes beyond simply enhancing local CO supply—for example, as demonstrated in a recently reported syngas-to-ethylene system[38]. In that study, the primary obstacle was CO dilution by H_2, which caused CO scarcity through external dilution, restricting CO transport to the catalyst surface and posing a transport-related barrier. The solution used COOH-functionalized carbon materials with enhanced CO adsorption energy to capture CO and increase its local concentration.

In this work, we tackle a distinct challenge: preserving high C_2H_4 selectivity when CO scarcity arises from internal consumption. Under such CO-depleted conditions, the competing HER becomes favourable over C–C coupling and the subsequent ethylene pathway. We therefore focus on modifying the catalyst's inherent properties to modulate the entire reaction process for improved C_2H_4 production

under a CO-starved environment. To this end, we designed nitrogen- and phosphorous-co-doped carbon (N,P-C) overlayers on the active Cu catalyst, which enhance CO adsorption and activation, facilitate the deoxygenation of the key intermediate *CHCOH and steer the reaction pathway towards ethylene. We implemented this concept in a zero-gap membrane electrode assembly (MEA) electrolyser and evaluated the performance under CO-starved conditions operated at high single-pass conversion. As a result, we simultaneously achieved a high C_2H_4 EE of 38% combined with a high C_2H_4 SPCE of 73% at 200 mA cm^{-2}, outperforming metrics seen in previous C_2H_4 electroproduction studies. Life cycle assessment shows that when CO_2 is sourced from direct air capture and energy is supplied using electricity having the carbon intensity of wind, the CO_2 emissions are reduced from today's +2.2 t CO_2e t^{-1} C_2H_4 to −2.5 t CO_2e t^{-1} C_2H_4, each cradle-to-gate. The overall energy cost of C_2H_4 production is 141 GJ t^{-1}, lower than that reported previously for C_2H_4 electroproduction.

Results

Catalyst design for C_2H_4 electrosynthesis

We first investigated the interplay between C_2H_4 EE and C_2H_4 SPCE in zero-gap MEA electrolyser systems by using a previously reported highly active and highly selective catalyst: Cu nanosheets[39]. In initial studies, we too witnessed a trade-off between C_2H_4 EE and C_2H_4 SPCE. Specifically, when we endeavoured to optimize C_2H_4 SPCE by lowering the CO flow rate at the inlet, we observed a decrease in C_2H_4 Faradaic efficiency (FE) alongside an increase in H_2 FE, ultimately resulting in a decline in C_2H_4 EE (Supplementary Figs. 1–3). This trade-off restricts the reduction in energy cost for C_2H_4 production (Supplementary Table 2).

We considered strategies to overcome this trade-off. At the outlet of a reactor operated at high SPCE, the catalyst becomes starved of CO because the reactant is substantially depleted at the catalyst surface. Under such CO-starved conditions, the local CO coverage on the catalyst surface diminishes, and the competing HER—which requires only protons and electrons—becomes kinetically favoured over the C–C coupling steps that lead to ethylene. Accordingly, we sought to orchestrate the full reaction pathway—from CO adsorption and activation to ethylene formation—under a CO-starved environment, which requires modifying the catalyst's inherent properties rather than merely enhancing local CO supply. This led us to seek catalysts that would enhance CO adsorption and activation, with the goal of promoting C–C coupling and steering reaction pathways towards C_2H_4 relative to HER (Fig. 2a).

Organic molecule additives, specifically those based on heteroatom-containing compounds, such as N-aryl-tetrahydro-bipyridine, cysteamine and N-heterocycle carbene, have been employed to modify catalysts to enhance CO adsorption and C–C coupling[40,41]. However, these improvements have typically been demonstrated under conditions with sufficient CO supply, not under the CO-starved environment that arises at high SPCE. Moreover, their long-term durability remains a concern[40].

We considered whether incorporating inorganic materials as modifiers onto the catalyst surface could unite enhanced catalytic performance with durability. Specifically, we looked into inorganic heteroatom-containing carbon materials that enable improvement in CO utilization, prioritizing both C–C coupling and the formation of intermediates to C_2H_4 and destabilizing undesired ones (Fig. 2b). As *CHCOH was identified to be a key intermediate in branching the C_2H_4 and ethanol pathway[42–44], we used density functional theory (DFT) calculations to study the reaction energies of the competing pathways, our purpose being to assess candidate inorganic heteroatom-containing modulator overlayers based on nitrogen-doped carbon (N-C) and phosphorous-doped carbon (P-C) (Supplementary Figs. 4–9). We found that thermodynamic preference of graphitic N is favoured over pyridinic and pyrrolic N (see details in DFT calculations in Methods); therefore, our calculations of activity and selectivity focus on graphitic N. We then calculated the reaction energies of *CHCOH to *CCH (ethylene pathway) and *CHCOH to *CHCHOH (ethanol pathway) (Fig. 2c) and found that P-C/Cu promotes C_2H_4 production, whereas N-C/Cu favours ethanol production compared with pristine Cu.

We then synthesized both P-C overlayer and N-C overlay catalysts (measured structure and composition in Supplementary Figs. 10–11), in each case atop Cu nanosheets, and evaluated COR performance (Fig. 2d). The N-C/Cu shifted ~20% FE from C_2H_4 to ethanol compared with Cu nanosheets (Supplementary Fig. 12). P-C/Cu showed a higher C_2H_4 FE than seen on pristine Cu (Supplementary Fig. 13). We calculated the ratios of C_2H_4 FE to ethanol FE ($FE_{ethylene}/FE_{ethanol}$) (Supplementary Fig. 14) and found that P-C/Cu showed the highest ratio of 15, compared to 0.9 for the N-C case. We used *operando* Raman on N-C/Cu and P-C/Cu (Supplementary Figs. 15–17). The peak (P1) at ~280 cm^{-1} is associated with the restricted rotation of adsorbed CO on Cu; and the peak (P2) in the range from 355 to 395 cm^{-1} with a Cu–CO stretch[45–47]. We observed that under the same potential, the bands for the Cu–CO stretch on the N-C/Cu showed an obvious blueshift compared with that on Cu, whereas the bands on P-C/Cu exhibited a slight blueshift compared with that on the Cu. The blueshift suggests stronger binding of CO with the N-C/Cu surface relative to Cu[47]. Thus, N-C overlap appears to facilitate preferential CO adsorption on the Cu surface, good for COR and suppressing competing HER.

We compared the HER performance and CO SPCE of N-C/Cu and P-C/Cu under the same flow rates of CO. N-C/Cu exhibits markedly greater resilience under CO-starved conditions compared to P-C/Cu: When the CO flow rate decreases, P-C/Cu shows a dramatic increase in H_2 FE and an appreciable decrease in C_2H_4 FE and C_2H_4 EE (Fig. 2e and Supplementary Fig. 18), whereas N-C/Cu maintains much lower HER activity and has a more consistent C_2H_4 FE and C_2H_4 EE, and simultaneously achieves substantially higher CO SPCE (Fig. 2f and Supplementary Figs. 19 and 20). However, under CO-starved conditions, both P-C/Cu and N-C/Cu suffer: P-C/Cu shows a notable decline in both C_2H_4 FE and C_2H_4 EE and an increase in H_2 FE, whereas N-C/Cu lacks sufficient selectivity to C_2H_4. Neither electrode offers therefore to reduce the energy cost of C_2H_4 production (Supplementary Tables 3 and 4).

We contemplated whether the benefits of P-doping (promoting the ethylene pathway) and N-doping (insensitivity to CO-starved conditions) could be combined. This led us to return to DFT. We found that a combined N,P-C/Cu catalyst may facilitate C–O cleavage of *CHCOH to favour ethylene production (Fig. 2c) and favour CO dimerization compared with pristine Cu (Fig. 2g).

Experimentally we fabricated N,P-C/Cu catalyst by incorporating an N,P-C overlayer on Cu nanosheet catalyst. We utilized a MOF@polymer pyrolysis approach (Fig. 3a). Electron microscopy of N,P-C shows a porous morphology (Fig. 3b,c), whereas the underlying Cu catalyst maintains its nanosheet structure (Fig. 3d). Energy-dispersive X-ray spectroscopy (EDS) elemental mapping displays a uniform dispersion of N, P and C (Fig. 3e). The coexistence of N, P and C is also seen in X-ray photoelectron spectroscopy (Supplementary Figs. 21 and 22). Cross-sectional scanning electron microscopy shows the N,P-C/Cu catalyst consists of two catalyst layers: the upper N,P-C layer and the lower Cu nanosheet layer (Fig. 3b). We acquired *operando* Cu K-edge X-ray absorption near-edge structure and extended X-ray absorption fine structure, whose spectra show that the Cu species of the N,P-C/Cu and Cu nanosheet are in the metallic state (Fig. 3f,g), as in Cu foil.

We used *operando* Raman under COR (Supplementary Figs. 23 and 24) as a function of applied potentials to study those intermediates that can be observed in this way. The D-band at 1,340 cm^{-1} and G-band at 1,590 cm^{-1} are seen in Raman spectra of N,P-C/Cu, which we index to the N, P co-doped C layer[48]. The Cu–CO peak at ~280 cm^{-1} and CO peak at ~2,100 cm^{-1} on N,P-C/Cu diminish at lower potentials compared with the case of pristine Cu; this suggests faster CO consumption on N,P-C/Cu. The blueshift of the Cu–CO peak observed on N,P-C/Cu suggests a stronger Cu–CO bond[47]. The N,P-C/Cu exhibited a higher ratio of P2 to P1, indicating enhanced C–C coupling on N,P-C/Cu[47]. The C–O

https://doi.org/10.1038/s41893-026-01849-0

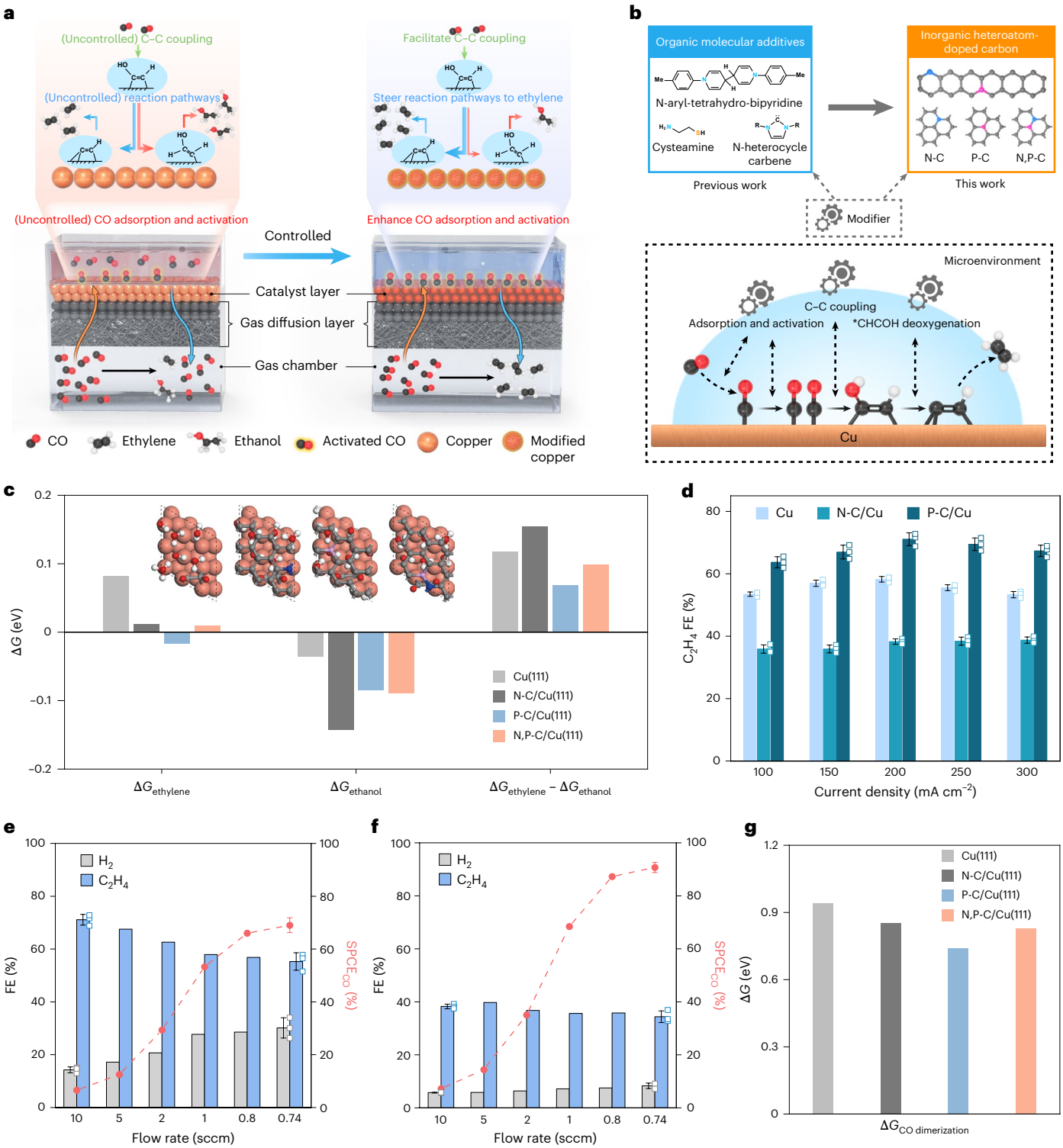

Fig. 2 | Ethylene electrocatalyst design. a, Schematic illustration of catalyst design strategy of modified Cu catalysts to simultaneously achieve both high C_2H_4 EE and high C_2H_4 SPCE in COR. This strategy seeks to enhance CO reactant coverage on the catalyst surface in CO-starved environments through facilitating CO adsorption and activation, prioritize C–C coupling over HER and steer the reaction pathways towards ethylene. **b**, Catalysts using inorganic heteroatom-containing carbon materials to replace organic molecular additives as modifiers; their purpose is to promote CO adsorption and activation, enhance C–C coupling and facilitate *CHCOH deoxygenation for enhanced C_2H_4 production. **c**, Reaction energies of the ethylene pathway (*CHCOH to *CCH) and the ethanol pathway (*CHCOH to *CHCHOH) on Cu(111), N-C/Cu(111), P-C/Cu(111) and N,P-C/Cu(111). **d**, C_2H_4 FE on different modified Cu electrodes (Cu nanosheet, N-C/Cu, and P-C/Cu) under different current densities. Values are means and error bars represent the standard deviation from three independent measurements. The corresponding data distribution is presented as hollow points. **e**,**f**, The performance of the P-C/Cu electrode (**e**) and the N-C/Cu electrode (**f**) under CO flow rates of 10, 5, 2 and 1 sccm in a 1-cm^2 MEA electrolyser and 4 and 3.7 sccm (equivalent to 0.8 and 0.74 sccm per cm^2 of normalized electrode area) in a 5-cm^2 MEA electrolyser at a constant current density of 200 mA cm^{-2}, respectively. Values are means and error bars represent the standard deviation from three independent measurements. The corresponding FE data distribution is presented as hollow points. **g**, Reaction energies of *CO dimerization on Cu(111), N-C/Cu(111), P-C/Cu(111) and N,P-C/Cu(111).

https://doi.org/10.1038/s41893-026-01849-0

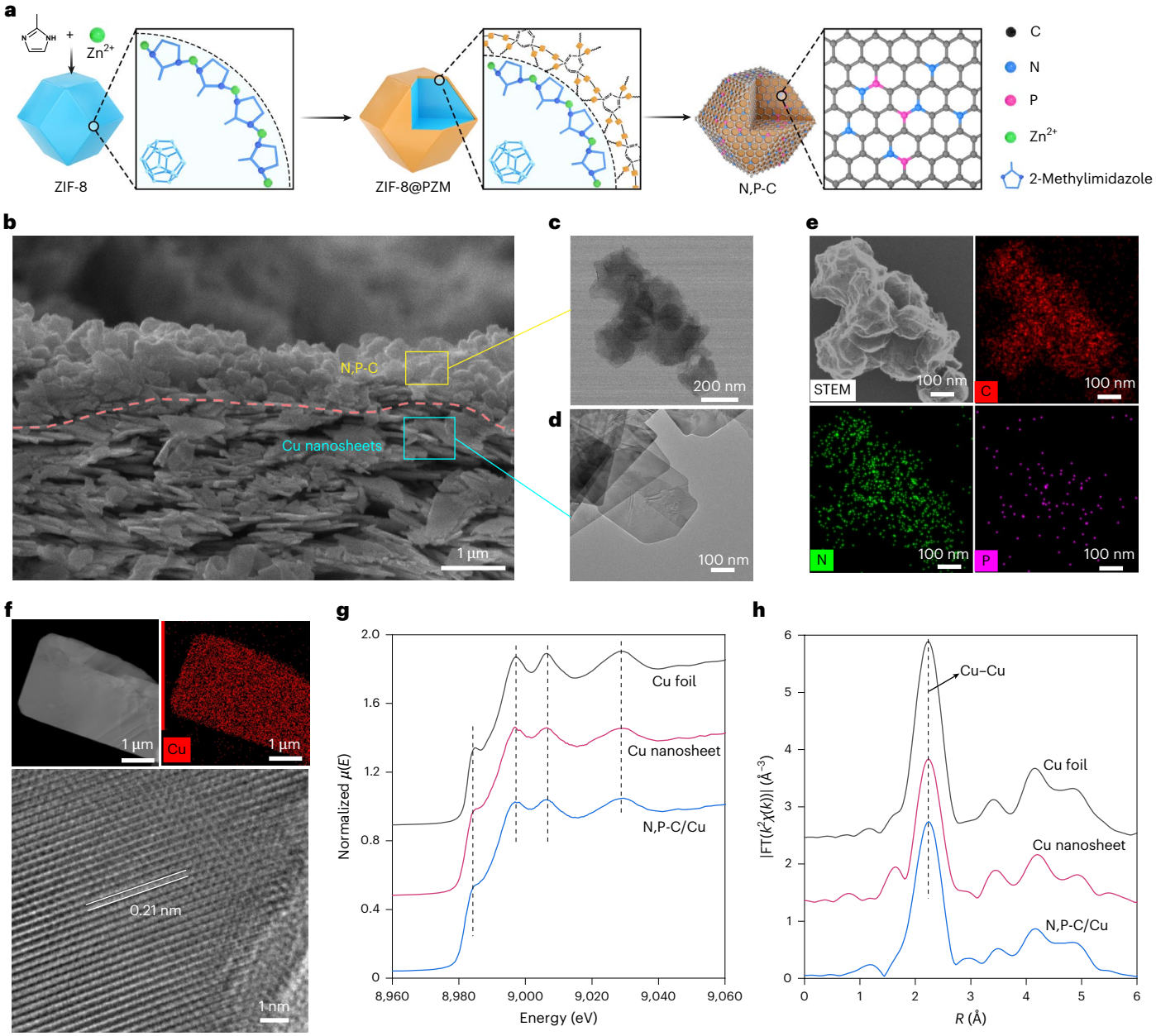

Fig. 3 | Structural characterization of the N,P-C/Cu catalyst. a, Schematic illustration of the synthesis process of N,P-C layer via a ZIF-8@polymer approach. ZIF-8 is zeolitic imidazolate framework-8. ZIF-8@PZM is a core-shell composition of poly-(cyclotriphospazene-co-4,4′-diaminodiphenylether) (PZM) coated onto ZIF-8. **b**, Cross-sectional scanning electron microscope (SEM) image of the N,P-C/Cu catalyst. **c**, Transmission electron microscope (TEM) image of upper N,P-C layer. **d**, Transmission electron microscope image of lower Cu nanosheet layer. **e**, Scanning transmission electron microscopy (STEM) image and the corresponding energy-dispersive X-ray spectroscopy (EDS) mapping images (C, red; N, green; P, pink) of the N,P-C layer. **f**, High-angle annular dark-field (HAADF)-STEM image and the corresponding EDS mapping as well as high-resolution transmission electron microscopy (HRTEM) image of Cu nanosheet. Each experiment was independently repeated at least three times with similar results for SEM (**b**), STEM and the corresponding EDS mapping (**e**) and HAADF-STEM and the corresponding EDS mapping (**f**). **g**, Cu K-edge X-ray absorption near-edge structure (XANES) spectra of the N,P-C/Cu, Cu nanosheet and Cu foil. **h**, Fourier-transformed (FT) magnitudes of Cu K-edge extended X-ray absorption fine structure (EXAFS) spectra of the N,P-C/Cu, Cu nanosheet and Cu foil. FT, Fourier transform; χ, EXAFS oscillation function; k, photoelectron wave number; μ, absorption coefficient; E, photon energy; R, radial distance.

stretching region at 1,900–2,100 cm^{-1} can be further deconvolved into three peaks ascribed to different adsorption configurations: bridge CO, the low-frequency band and the high-frequency band linear CO, which are located at approximately 2,030 cm^{-1}, 2,060 cm^{-1} and 2,090 cm^{-1}, respectively[49]. Low-frequency band CO is typically associated with adsorbed CO intermediates that favours C–C coupling[49]. Raman spectra of N,P-C/Cu exhibited a dominance of low-frequency band CO, which is higher than those of the pristine Cu (Supplementary Figs. 25–27). These *operando* Raman results suggest that the N,P-C layer increases CO adsorption and facilitates the C–C coupling of the adsorbed CO, as also seen in DFT.

Electrocatalytic performance in zero-gap MEA electrolyser systems

We investigated electrocatalytic performance of N,P-C/Cu, comparing to controls of N-C/Cu, P-C/Cu and Cu electrodes, evaluating C_2H_4 FE and C_2H_4 partial current density versus applied potential (Supplementary Figs. 28–31 and Supplementary Note 7). N,P-C/Cu

https://doi.org/10.1038/s41893-026-01849-0

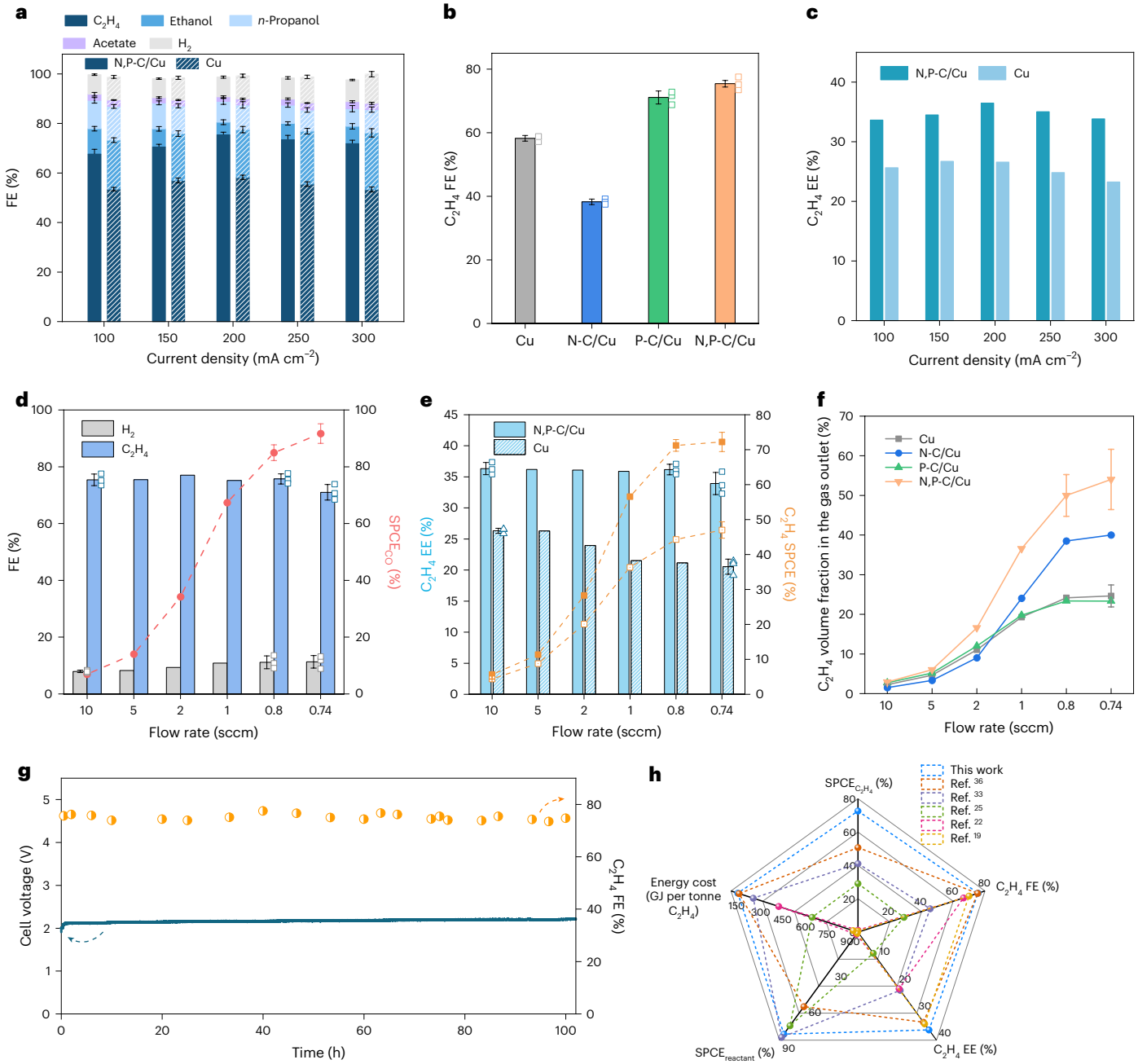

Fig. 4 | Ethylene electrosynthesis performance. a, FEs of COR products on N,P-C/Cu electrode and the pristine Cu electrode (the hatched bars) under different current densities. Values are means and error bars represent the standard deviation from three independent measurements. **b**, Comparison of C_2H_4 FE on different modified Cu electrodes at 200 mA cm^{-2}. Values are means, and error bars represent the standard deviation from three independent measurements. The corresponding data distribution is presented as hollow points. **c**, C_2H_4 energy efficiency of the N,P-C/Cu and the pristine Cu electrodes. **d**, H_2 FE, C_2H_4 FE, SPCE of CO on N,P-C/Cu electrode under CO flow rates of 10, 5, 2 and 1 sccm in a 1-cm^2 MEA electrolyser and 4 and 3.7 sccm (equivalent to 0.8 and 0.74 sccm per cm^2 of normalized electrode area) in a 5-cm^2 MEA electrolyser at a constant current density of 200 mA cm^{-2}, respectively. Values are means, and error bars represent the standard deviation from three independent measurements. The corresponding FE data distribution is presented as hollow points. **e**, C_2H_4 EE and C_2H_4 SPCE on the pristine Cu nanosheet electrode under CO flow rates of 10, 5, 2 and 1 sccm in a 1-cm^2 MEA electrolyser and 4 and 3.7 sccm (equivalent to 0.8 and 0.74 sccm per cm^2 of normalized electrode area) in a 5-cm^2 MEA electrolyser at a constant current density of 200 mA cm^{-2}, respectively. Values are means, and error bars represent the standard deviation from three independent measurements. The corresponding C_2H_4 EE data distribution is shown as hollow points: hollow squares for N, P/C-Cu, and hollow triangles for Cu. **f**, C_2H_4 volume fraction in the gas outlet on the N,P-C/Cu, P-C/Cu, N-C/Cu and Cu electrodes under CO flow rates of 10, 5, 2 and 1 sccm in a 1-cm^2 MEA electrolyser and 4 and 3.7 sccm (equivalent to 0.8 and 0.74 sccm per cm^2 of normalized electrode area) in a 5-cm^2 MEA electrolyser at a constant current density of 200 mA cm^{-2}, respectively. Values are means, and error bars represent the standard deviation from three independent measurements. **g**, The stability test of the N,P-C/Cu electrode during 100 h operation of COR at a constant current density of 200 mA cm^{-2}. **h**, Comparison of the C_2H_4 SPCE, FE and EE of C_2H_4, SPCE of reactant, and energy consumption for C_2H_4 production of the N,P-C/Cu electrode in this work with those of state-of-the-art electrodes[19,22,25,33,36].

exhibited the highest C_2H_4 FE of 75% at −1.3 V versus RHE with a C_2H_4 partial current density of 190 mA cm^{-2}. We then deployed the N,P-C/Cu in a zero-gap MEA electrolyser (Fig. 4a–c). It achieved C_2H_4 FE of 75% ± 2% at 200 mA cm^{-2} with a 36% C_2H_4 EE (Fig. 4b,c, Supplementary Figs. 32–37 and Supplementary Note 8). This C_2H_4 EE value surpasses that seen in earlier reports (Fig. 1d and Supplementary Table 5). The ratios of C_2H_4 FE to ethanol FE ($FE_{ethylene}/FE_{ethanol}$) were calculated to estimate the selectivity towards C_2H_4 versus ethanol in COR (Supplementary Fig. 38). In comparison to the pristine Cu, the N,P-C/Cu and the P-C/Cu show higher $FE_{ethylene}/FE_{ethanol}$, whereas the N-C/Cu exhibits lower $FE_{ethylene}/FE_{ethanol}$, in agreement with the DFT calculations, indicating that the N,P-C layer covering on Cu favours the C_2H_4 pathway.

We then pursued high CO SPCE; the N,P-C/Cu achieved a value of 92% ± 3%: This corresponds to 72% of carbon atoms going to C_2H_4, and it was achieved simultaneously with 34% ethylene EE (Fig. 4d,e), an advance in the EE:SPCE combination over earlier reports in both CO_2R and COR systems (Fig. 1d and Supplementary Table 5). N,P-C/Cu also exhibited higher C_2H_4 EE and C_2H_4 SPCE than did either P-C/Cu or N-C/Cu (Supplementary Figs. 39 and 40 and Supplementary Note 9). We also assessed the C_2H_4 volume fraction in the gas outlet of our system. We achieve a C_2H_4 volume fraction of 54% ± 8%, the highest reported among COR systems (Fig. 4f and Supplementary Fig. 41). To assess stability, we studied 100-hour operation in the MEA electrolyser (Fig. 4g): both voltage and FE changed no more than 7% (relative) over this duration of operation. Our energy analysis suggests that the performance achieved in the N,P-C/Cu electrode system provides an estimated energy intensity of C_2H_4 production of 145 GJ t^{-1}, which is lower than that of the highest-efficiency prior C_2H_4 electrosynthesis[36]; comparing both with the cascade CO_2-to-CO followed by CO-to-C_2H_4 approach[33,36] and with direct CO_2R, including alkaline CO_2R[19], neutral CO_2R[22,24] and acidic CO_2R systems[25,26] (Figs. 4h and Fig. 5a, Supplementary Notes 1–4 and Supplementary Table 6). We estimate that, when the CO_2 feedstock is obtained through direct air capture and wind electricity is employed, the cradle-to-gate carbon intensity reaches −2.6 t CO_2e t^{-1} C_2H_4, in contrast to today's value of +2.2 t CO_2e t^{-1} C_2H_4 (Supplementary Fig. 42).

Mechanistic insights and catalyst optimization

We conducted electrochemical analysis to investigate further the function of the inorganic heteroatom-doped carbon overlay (Supplementary Note 10). We measured Tafel slopes of four catalysts, including Cu, N-C/Cu, P-C/Cu and N,P-C/Cu (Supplementary Fig. 43). These exhibit Tafel slope values of ~120 mV dec^{-1}, indicating that water is involved in the rate-determining step of the CO-to-C_2H_4 pathway. We carried out D_2O experiments and kinetic isotope effect analysis (Supplementary Figs. 44 and 45). The kinetic isotope effect values (1.8–2.1 for Cu and N-C/Cu and 1.3–1.7 for P-C/Cu and N,P-C/Cu) also indicate the involvement of water in the rate-determining step of C_2H_4 formation (Supplementary Fig. 46). The results agree with a picture in which increasing interfacial water concentration and accelerating water dissociation favour ethylene production.

We then evaluated the catalytic performance of the N,P-C/Cu electrode in different electrolytes consisting of different alkali ions, including 1 M LiOH, 1 M NaOH and 1 M KOH (Supplementary Figs. 47 and 48). The C_{2+} FE follows the order 1 M LiOH < 1 M NaOH < 1 M KOH (Supplementary Fig. 48a). This finding is consistent with previous reports that larger alkali cations ($K^+ > Na^+ > Li^+$) enhance C–C coupling and suppress HER in both CO_2R and COR systems, a finding linked to their strong electric field effects, which enable higher C_{2+} selectivity. However, in our work, we observed a distinct ethylene selectivity trend: 1 M LiOH > 1 M NaOH > 1 M KOH (Supplementary Fig. 48b). Among hydrated cations (K^+, Na^+, Li^+), Li^+ possesses the largest hydration shell size, consistent with enhanced interfacial water availability contributing to superior C_2H_4 selectivity.

We also noted that P doping in the carbon-based overlayers (that is P-C and N,P-C) leads to lower kinetic isotope effect (KIE) values, indicating that the P doping accelerates the water dissociation process (Supplementary Fig. 46). These observations, together with the above DFT calculations and *operando* Raman spectra, suggest that N species enhance CO adsorption and that P species support C–C coupling to form C_2 intermediates and facilitate water dissociation that enhances the hydrogenation of the C_2 intermediate to generate C_2H_4.

We sought a synthetic strategy to enable independent control over the doping of N versus P species. To do this, we prepared N,P-C overlayers via two distinct synthetic routes (Supplementary Figs. 49–51, Supplementary Table 7 and Supplementary Note 11). Compared to the synthetic approach employed up to this point, we find that when the N/P ratio is similar, the ethylene FE and C_2H_4-to-ethanol FE ratios are substantially similar (Supplementary Figs. 52–54).

When we employed an N,P-C overlayer with an optimized N/P ratio of 3.1 to construct the optimal N,P-C/Cu electrode (Opti-N,P-C/Cu), we reached a C_2H_4 FE of 77% and a C_2H_4 EE of 38% (Supplementary Figs. 55 and 56). When optimized for single-pass carbon utilization, this led to a CO SPCE of 92% ± 2% (Supplementary Fig. 55), resulting in a C_2H_4 volume fraction in the gas outlet of 56% ± 4% (Supplementary Fig. 57), which surpasses that of earlier reports (Supplementary Fig. 58). We estimate that our catalyst system achieves an overall energy cost of 141 GJ t^{-1} C_2H_4 (Supplementary Table 8).

Energy cost analysis and sensitivity analysis

We conducted energy cost analysis to study the role of integrated optimization of both catalyst and system. On the pristine Cu electrode, the trade-off between C_2H_4 EE and SPCE leads to a constraint on the overall energy cost of ethylene production. Specifically, attempts to reduce downstream separation costs by improving C_2H_4 SPCE lead to a decline in C_2H_4 EE, and this increases the energy demand of electrolysis. The total energy cost of C_2H_4 production then increases from 229 to 232 GJ t^{-1} (Fig. 5a). This trade-off limits the C_2H_4 volume fraction in the gas outlet to less than ~30% (Fig. 5b). In contrast, using the catalyst studied herein, we increase the C_2H_4 EE in a way that reduces both the electrolysis energy and the required CO input (Supplementary Fig. 59). When we then optimize the system towards higher SPCE, the N,P-C/Cu electrode maintains its high EE. This concurrent improvement in EE and SPCE reduces the separation energy, yielding an overall energy cost of 145 GJ t^{-1} C_2H_4 (Fig. 5a). Further optimization of the N,P-C overlayer composition to construct the Opti-N,P-C/Cu electrode further lowers this value to 141 GJ t^{-1}. The C_2H_4 outlet volume fraction reaches 56% ± 4% (Fig. 5b).

We put these results in context by comparing the energy costs of leading ethylene electrosynthesis routes (Fig. 5c). Alkaline and neutral CO_2R systems achieve high C_2H_4 EE (~30%) but suffer carbon losses to (bi)carbonate, limiting SPCE to <25%. The energy penalties associated with CO_2 regeneration from carbonate in alkaline media or from anode-stream recycling in neutral configurations add substantial costs. Acidic CO_2R systems improve SPCE but at the expense of EE (<20%) due to severe hydrogen evolution, leading to increased electrolysis costs. By breaking the EE–SPCE trade-off, we reduce electrolysis energy, product separation energy and the required CO input cost, where the latter embeds the energy cost from upstream CO_2 capture via direct air capture and CO generation via solid oxide electrolysis cell. Taken together these benefits lead to better total energy compared to both direct CO_2R pathways and alkaline COR benchmarks. The system also delivers a higher C_2H_4 outlet volume fraction in these benchmarks (Fig. 5d).

A sensitivity analysis was performed to show the pathway for future improvement. Given the measured high-CO single-pass conversion herein, further reductions in the overall energy cost for C_2H_4 electrosynthesis can be realized by optimizing C_2H_4 FE, solid oxide electrolysis cell capital and operating costs, full-cell voltage and CO_2-capture expenses (Fig. 5e). The system exhibits greater resilience to the carbon intensity of the electricity supply[50]: The cradle-to-gate

https://doi.org/10.1038/s41893-026-01849-0

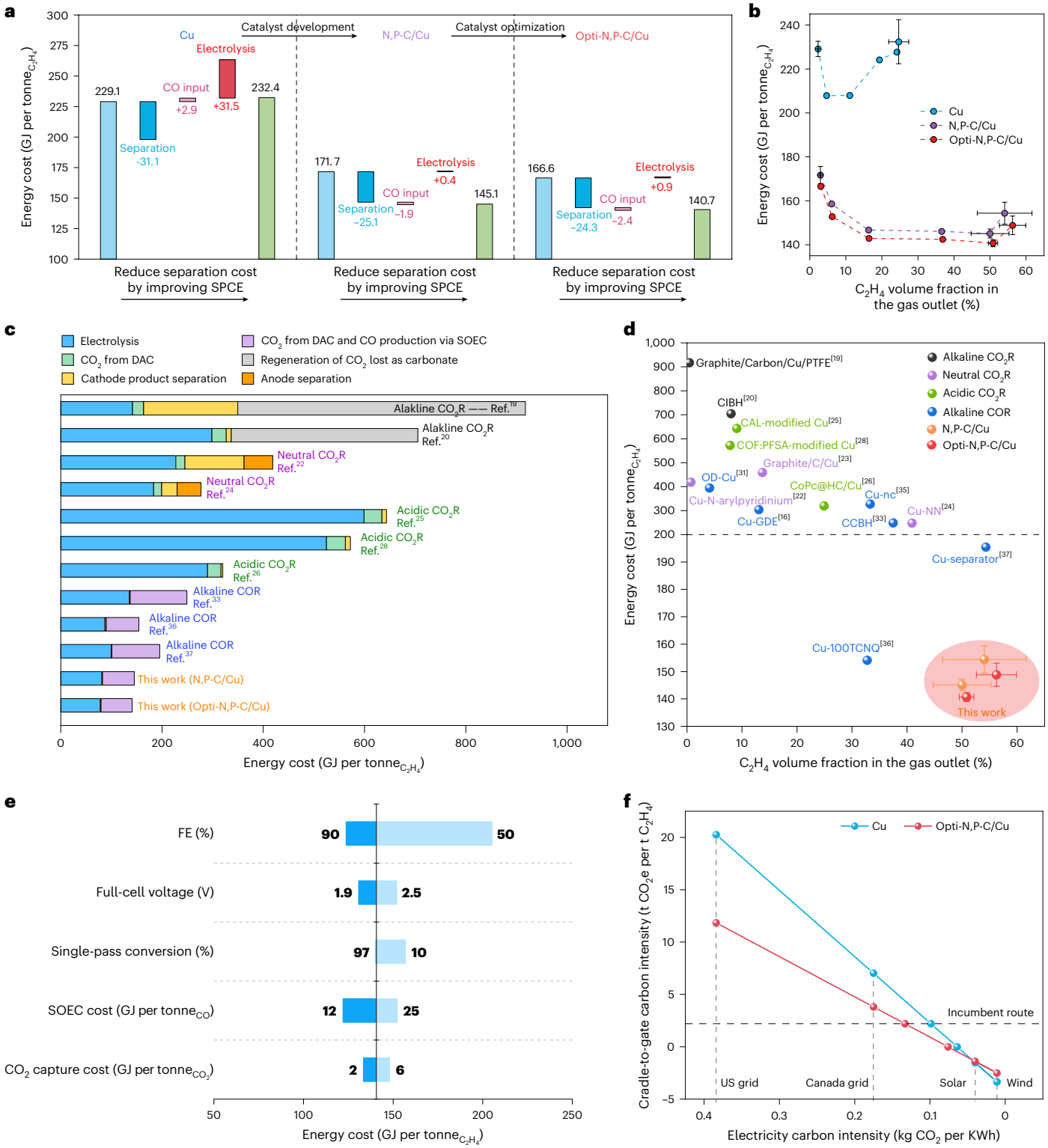

Fig. 5 | System energy analysis and sensitivity analysis for electrified synthesis of ethylene. a, Analysis and comparison of system energy consumption of ethylene electrosynthesis on the pristine Cu, N,P-C/Cu and Opti-N,P-C/Cu electrodes. Separation corresponds to the energy required for downstream product separation; CO input corresponds to the energy cost from upstream CO_2 capture (via direct air capture) and CO generation (via solid oxide electrolysis cell); and electrolysis corresponds to the energy required for the CO-to-C_2H_4 conversion. **b**, Comparison of system energy cost and ethylene outlet volume fraction on the pristine Cu, N,P-C/Cu and Opti-N,P-C/Cu electrodes. Values are means and error bars represent the standard deviation from three independent measurements. **c**,**d**, Estimated energy consumption for ethylene electrosynthesis (**c**) and ethylene outlet volume fraction (**d**) based on this work and state-of-the-art CO_2R and COR systems, including alkaline CO_2R, neutral CO_2R, acidic CO_2R and alkaline COR. Values are means and error bars represent the standard deviation from three independent measurements. **e**, Sensitivity analysis for the energy consumption for ethylene electrosynthesis. Data for these calculations are from experimental results of Opti-N,P-C/Cu electrode presented in this work. **f**, Estimated cradle-to-gate carbon intensity of ethylene electrosynthesis based on the pristine Cu and Opti-N,P-C/Cu electrode systems with electricity carbon intensity.

carbon intensity remains lower than that of the incumbent C_2H_4 production route when the grid carbon intensity is below 0.13 kg CO_2 kWh^{-1}, whereas the pristine Cu electrode requires a carbon intensity below 0.1 kg CO_2 kWh^{-1} to match the same benefit (Fig. 5f).

Discussion

This work reports inorganic heteroatom-doped carbon overlayers as modifiers to overcome the trade-off between C_2H_4 EE and C_2H_4 SPCE in ethylene electrosynthesis. Breaking this trade-off is important because it addresses the conflict between electrolysis energy cost and downstream separation energy—two factors that together dominate the overall energy cost of electrochemical ethylene production. By designing and then optimizing inorganic N,P-C overlayers on Cu nanosheet catalysts in zero-gap MEA electrolysers, we simultaneously achieved a high C_2H_4 EE of 38% along with a high C_2H_4 SPCE of 73% at 200 mA cm^{-2}, resulting in a total energy cost of C_2H_4 production of 141 GJ t^{-1}, lower than previous ethylene electrosynthesis benchmarks. Life cycle assessment indicates the potential to contribute to decarbonizing ethylene production when coupled with low-carbon electricity and CO_2 from direct air capture.

The source of CO feedstock critically shapes the requirements for catalyst and system design in CO-to-ethylene electrosynthesis. When CO is derived from industrial syngas, catalyst and system designs that address H_2 dilution become essential, as exemplified by recently reported syngas-to-ethylene work[38]. By contrast, when CO is produced via electrochemical CO_2-to-CO conversion technologies such as solid oxide electrolysis cells, the resulting CO stream is pure and well-suited for a fully electrified cascade process: CO_2 is first electrochemically converted to CO, followed by CO-to-C_2H_4 electrosynthesis. For this scenario, the present study offers an optimized solution that enables energy-efficient electrified ethylene synthesis with reduced overall energy cost by simultaneously achieving high C_2H_4 EE and C_2H_4 SPCE.

A fundamental insight into the differences is that whereas both systems face conditions of low CO availability, the root cause of CO scarcity is different, dictating distinct solution strategies. In the syngas work, CO scarcity arises from external dilution: The coexistence of H_2 and CO limits CO transport to the catalyst surface, creating a mass transport problem. The solution employs a COOH-functionalized carbon material that selectively captures CO from syngas and enhances CO adsorption on Cu, thereby transporting CO preferentially over H_2 to the catalytic sites. That strategy focuses on the adsorption and enrichment of CO reactant to overcome transport limitations. In the present work, CO scarcity arises from internal depletion: High single-pass conversion consumes CO along the flow channel, leaving the catalyst surface CO-starved. This is an intrinsic kinetic problem, as the competing HER becomes favoured when local CO coverage is low. Rather than enhancing local CO supply, we target the intrinsic catalytic properties of the catalyst itself. Our N,P-C overlayer design performs multiple synergistic functions: Nitrogen species enhance CO adsorption and impart resilience under CO-starved conditions; phosphorus species accelerate water dissociation and promote C–C coupling; together, they facilitate the deoxygenation of the key intermediate *CHCOH, steering the reaction pathway towards C_2H_4. This holistic modulation of the entire reaction process enables the simultaneous achievement of high C_2H_4 EE and high C_2H_4 SPCE.

Together, these two studies provide a complementary toolkit for sustainable ethylene electrosynthesis across the two primary CO feedstock scenarios: One enables direct utilization of abundant but dilute industrial syngas, whereas the other maximizes performance in a fully electrified cascade from CO_2. Collectively, they advance the broader goal of decarbonizing chemical production through electrification by addressing the challenges posed by different CO sources.

Despite these advances, several limitations remain on the path to practical deployment. Looking ahead, further work is required to study extended operation over industrially relevant timescales and scales, along with assessment under realistic process conditions that include impurity loads, membrane and electrode behaviour, and integrated water and heat management.

Methods

Chemicals

Zinc nitrate hexahydrate (98%), cupric chloride, lithium hydroxide, 2-methylimidazole (98%), methanol, ethanol, N, N-dimethylformamide, triethylamine, Nafion perfluorinated resin solution (5 wt% in a mixture of lower aliphatic alcohols and water), sodium hydroxide, potassium hydroxide, deuterium oxide, dimethyl sulfoxide, glucose, sodium hypophosphite, nickel(II) nitrate hexahydrate, iron(III) nitrate nonahydrate, NH_4F, urea and hydrochloric acid were purchased from Sigma Aldrich. Phosphonitrilic chloride trimer (98%) and bis(4-aminophenyl) ether (98%) were purchased from Alfa Aesar. Sustainion anion-exchange membrane was purchased from Dioxide Materials. Nickel foam and gas-diffusion layer (Freudenberg H23C3) and carbon powder (Vulcan XC-72R) were obtained from the Fuel Cell Store. The distilled water with a resistivity of 18.2 MΩ cm obtained from a Milli-Q reference water-purification system was used to prepare the aqueous solutions in all the experiments. All chemicals were used without any further purification.

Synthesis of N,P-C, N-C and P-C layers

N,P-C material was synthesized via MOF@ploymer pyrolysis approach through the pyrolysis of ZIF-8@ploymer composition. For the synthesis of ZIF-8, 24 mmol of 2-methylimidazole was dissolved in 100 ml of methanol and then added to 100 ml of methanol solution containing 6 mmol of $Zn(NO_3)_2{\cdot}6H_2O$. The mixture was vigorously stirred for 3 min and then kept at 35 °C for 6 h. The ZIF-8 precipitate was washed with methanol and dried in a vacuum. For the synthesis of ZIF-8@PZM, the 400 mg of as-obtained ZIF-8 powder was sonicated and dispersed in 40 ml of methanol, then added to 100 ml of methanol solution containing 320 mg of bis(4-aminophenyl) ether and 152 mg of phosphonitrilic chloride trimer. Then, 1 ml of triethylamine was added dropwise to the above-formed mixture solution, which was vigorously stirred for 15 h to induce the polymerization. Subsequently, the sample was washed with methanol, dried overnight in the vacuum and collected as ZIF-8@PZM. The as-fabricated ZIF-8@PZM was pyrolyzed in Ar at a heating flow rate of 5 °C min^{-1} to 950 °C, with the target temperature held for 3 h, to obtain N,P-C material. The optimal N,P-C material was synthesized using a procedure similar to that of the aforementioned N,P-C material, but with 640 mg of bis(4-aminophenyl) ether and 304 mg of phosphonitrilic chloride trimer. N-C material was synthesized by the pyrolysis of ZIF-8 in Ar at a heating flow rate of 5 °C min^{-1} to 950 °C, with the target temperature held for 3 h. In a typical synthesis of P-C material, 1.2 g of glucose was dissolved in 80 ml of deionized water, then transferred to 100-ml Teflon-lined stainless-steel autoclave and maintained at 180 °C for 12 h. Then, the precipitate was washed, dried and pyrolyzed in an Ar atmosphere at 700 °C for 2 h at a heating flow rate of 5 °C min^{-1} to obtain the carbon sphere. Subsequently, 0.75 g of $NaH_2PO_2{\cdot}H_2O$ in a porcelain boat was placed at the front part of the tube furnace, and 0.05 g of carbon sphere in a porcelain boat was placed at the centre of the tube furnace, followed by the pyrolysis at 400 °C for 1 h at a heating flow rate of 2 °C min^{-1} under an Ar atmosphere to obtain P-C material. The detailed synthesis procedures of N,P-C materials with different contents of N and P via MOF@polymer pyrolysis approach and pyrolysis-phosphorization approach are shown in Supplementary Fig. 49 and Supplementary Note 11.

Synthesis of Cu nanosheet

First, 3 mmol of anhydrous $CuCl_2$ was dissolved in 50 ml of deionized water and sonicated for 15 min. Then, 10 ml of deionized water containing 7.2 g of NaOH was added dropwise. The mixture solution

was vigorously stirred for 15 min and then transferred to a 100-ml Teflon-lined stainless-steel autoclave and maintained at 100 °C for 12 h. The precipitate was washed with deionized water and dried in a vacuum to obtain CuO nanosheet. The Cu nanosheet catalyst was prepared by in situ CO electroreduction of CuO nanosheet loaded on gas-diffusion electrode under 50 mA cm^{-2} for 30 min.

Electrode preparation

The N,P-C/Cu electrode was prepared through airbrushing the catalyst ink consisting of 20 mg of CuO nanosheet, 4 ml methanol and 60 µl Nafion perfluorinated resin solution onto a conductive gas-diffusion layer (carbon paper, Freudenberg H23C3) with a CuO nanosheet loading of 1 mg cm^{-2}. Then, the catalyst ink containing 2 mg of N,P-C, 2 ml methanol and 6 µl Nafion perfluorinated resin solution was sprayed on the CuO nanosheet with a N,P-C loading of 0.1 mg cm^{-2}. The N-C/Cu and P-C/Cu electrode were prepared following the same procedure for the N,P-C/Cu electrode, except that N,P-C was replaced by N-C and P-C, respectively.

Material characterization

X-ray powder diffractometer data were collected in a MiniFlex600 with Cu-Kα radiation. Scanning electrode microscopy measurements were performed in a Hitachi FE-SEM SU 5000 microscope. Transmission electron microscopy and energy-dispersive X-ray spectroscopy measurements were carried out on a JEOL JEM-2100F with an electron acceleration energy of 200 kV. HAADF-STEM images were obtained on a high-resolution transmission electron microscopy (JEM-ARM200F working at 300 kV). X-ray photoelectron spectroscopy data were collected in an ECSA device (PHI 5700) with Al Kα X-ray energy source (1,486.6 eV) for excitation. X-ray absorption spectroscopy measurements were performed with a modified flow cell in Soft X-ray Micro-Characterization Beamline (SXRMB) at the Canadian Light Source (Saskatoon, Canada), which is equipped with a water-cooled Si (111) and InSn (111) double-crystal monochromator covering a photo energy range from 1.7 to 10.0 keV. Analyses of the XAS data was carried out using ATHENA and ARTEMIS software incorporated into a standard IFEFFIT package. *Operando* Raman data were collected in a Renishaw inVia Raman Microscope with a water immersion objective (×63) and a 785-nm laser in a modified flow cell.

DFT calculations

All ab initio DFT calculations were conducted using the projector-augmented-wave method as implemented in the Vienna Ab initio Simulation Package[51,52], employing the Perdew–Burke–Ernzerhof parametrization[53] for the exchange-correlation function within the generalized gradient approximation. All calculations consistently used a plane-wave cutoff of 450 eV and 3 × 3 × 1 gamma-centred *k*-point grids generated by the Monkhorst–Pack scheme[54]. To account for field and solvation effects and long-range van der Waals interactions, a charged water overlayer[55] together with the zero-damping DFT-D3 method of Grimme[56] was incorporated. The water structure was optimized using ab initio molecular dynamics simulations in a constant-volume, constant-temperature ensemble for 10 ps with a time step of 0.5 fs at 300 K using the Nosé–Hoover thermostat. Copper was modelled using the (111) facet with a hexagonally charged water overlayer, comprising five water molecules and a hydronium (H_3O^+) ion. A vacuum region exceeding 15 Å in thickness was included perpendicular to the surfaces to prevent artificial interactions. During structural optimization, atoms in the bottommost two layers were fixed, whereas the remaining atoms and adsorbates were allowed to relax.

We performed DFT calculations to evaluate the formation energies of the three major nitrogen species observed experimentally—graphitic, pyrrolic and pyridinic N—when doped into a 4 × 4 graphene. Our results indicate that graphitic N exhibits the lowest formation energy among the three (1.24, 6.21 and 9.22 eV for graphitic, pyridinic and pyrrolic N, respectively), suggesting it is the most thermodynamically favourable configuration under the synthesis conditions and, therefore, the most likely to dominate in the N,P-C layer.

Electrochemical measurement

The COR measurements were performed in an MEA electrolyser. The cathode catalyst was attached to the cathode side. The activated Sustainion membrane and a homemade NiFeP foam[57] were placed on the top of the cathode successively and then assembled in MEA. On the anode side, 1 M LiOH aqueous solution was used as the anolyte and was circulated using a pump. On the cathode side, CO gas flowed to the humidifier with deionized water and was then supplied to the cathode chamber of the MEA. The performance of the catalysts in the MEA system was assessed in the two-electrode system at the electrochemical station (Autolab PGSTA204) equipped with a current boost (Metrohm Autolab, 10 A). In all the electrochemical tests, the gas products were analysed using a gas chromatograph (Shimadzu GC-2014, PerkinElmer Clarus 580). The liquid products were measured by 1H nucleo-magnetic resonance spectroscopy (600 MHz Agilent DD2 NMR Spectrometer) with dimethyl sulfoxide (DMSO) as the reference standard and deuterium oxide (D_2O) as the lock solvent.

The full-cell EE based on the production of ethylene was calculated using the following equation:

$$EE_{fullcell,ethylene} = \frac{(1.23 + (-E^0_{ethylene})) \times FE_{ethylene}}{E_{fullcell}}$$

where $E^0_{ethylene}$ ($E^0_{ethylene}$ = 0.17 V versus RHE) is the thermodynamic potential of CO to ethylene, $FE_{ethylene}$ is the FE value of ethylene and $E_{full\ cell}$ is the full-cell voltage without ohmic loss correction measured in MEA system.

At the conditions of 298.15 K and 101.3 kPa, the CO SPCE is calculated as follows:

$$SPCE_{CO} = 60\left(\frac{s}{min}\right) \times \sum \frac{\text{Current (A)} \times FE_i \times \text{Molar ratio}\left(\frac{CO}{product_i}\right)}{N_i \times F} \times \frac{8.314\ (\text{J mol}^{-1}\text{K}^{-1}) \times 298.15\ (\text{K})}{101300\ (\text{Pa})} \div V_{CO\ feed\ rate}\left(\frac{m^3}{min}\right)$$

Where current is the total current; FE_i is the measured FE (%) of the product *i*; N_i is electrons transferred for product *i*; F is Faraday's constant. $V_{CO\ feed\ rate}$ is the flow rate of CO at the inlet.

C_2H_4 SPCE is calculated as follows:

$$SPCE_{ethylene} = 60\left(\frac{s}{min}\right) \times \frac{\text{Current (A)} \times FE_{ethylene} \times \text{Molar ratio}\left(\frac{CO}{ethylene}\right)}{N_{ethylene} \times F} \times \frac{8.314\ \left(\text{J mol}^{-1}\text{K}^{-1}\right) \times 298.15\ (\text{K})}{101300\ (\text{Pa})} \div V_{CO\ feed\ rate}\left(\frac{m^3}{min}\right)$$

The volume fraction of a gas in the outlet is calculated as follows:

$$\varphi_i = \frac{V_i}{V_{total}}$$

Where V_i is the partial volume of gas product *i* in the outlet and V_{total} is the total volume of the gas mixture in the outlet.

The calculation details of C_2H_4 volume fraction in the gas outlet is shown in Supplementary Note 6.

Reporting summary

Further information on the research design is available in the Nature Portfolio Reporting Summary linked to this article.

Data availability

The data supporting this study are available within the paper and the Supplementary Information. Source data are provided with this paper.

References

1. Leow, W. R. et al. Chloride-mediated selective electrosynthesis of ethylene and propylene oxides at high current density. *Science* **368**, 1228–1233 (2020).
2. Achakulwisut, P. et al. Global fossil fuel reduction pathways under different climate mitigation strategies and ambitions. *Nat. Commun.* **14**, 5425 (2023).
3. Geyer, R., Jambeck, J. R. & Law, K. L. Production, use, and fate of all plastics ever made. *Sci. Adv.* **3**, e1700782 (2017).
4. Gao, Y. et al. Recent advances in intensified ethylene production – a review. *ACS Catal.* **9**, 8592–8621 (2019).
5. Amghizar, I. L., Vandewalle, L. A., Van Geem, K. M. & Marin, G. B. New trends in olefin production. *Engineering* **3**, 171–178 (2017).
6. Ren, T., Patel, M. K. & Blok, K. Steam cracking and methane to olefins: energy use, CO_2 emissions and production costs. *Energy* **33**, 817–833 (2008).
7. Shen, W., Tian, Z., Zhao, L. & Qian, F. Life cycle assessment and multiobjective optimization for steam cracking process in ethylene plant. *ACS Omega* **7**, 15507–15517 (2022).
8. *The Future of Petrochemicals* (IEA, 2018); https://www.iea.org/reports/the-future-of-petrochemicals
9. De Luna, P. et al. What would it take for renewably powered electrosynthesis to displace petrochemical processes? *Science* **364**, eaav3506 (2019).
10. Zhong, M. et al. Accelerated discovery of CO_2 electrocatalysts using active machine learning. *Nature* **581**, 178–183 (2020).
11. Chen, Y. et al. Catalyst design for electrochemical CO_2 reduction to ethylene. *Matter* **7**, 25–37 (2024).
12. Shin, H., Hansen, K. U. & Jiao, F. Techno-economic assessment of low-temperature carbon dioxide electrolysis. *Nat. Sustain.* **4**, 911–919 (2021).
13. Ozden, A. et al. Carbon-efficient carbon dioxide electrolysers. *Nat. Sustain.* **5**, 563–573 (2022).
14. Rabinowitz, J. A. & Kanan, M. W. The future of low-temperature carbon dioxide electrolysis depends on solving one basic problem. *Nat. Commun.* **11**, 5231 (2020).
15. Chen, C., Li, Y. & Yang, P. Address the 'alkalinity problem' in CO_2 electrolysis with catalyst design and translation. *Joule* **5**, 737–742 (2021).
16. Ripatti, D. S., Veltman, T. R. & Kanan, M. W. Carbon monoxide gas diffusion electrolysis that produces concentrated C_2 products with high single-pass conversion. *Joule* **3**, 240–256 (2019).
17. Jouny, M., Luc, W. & Jiao, F. General techno-economic analysis of CO_2 electrolysis systems. *Ind. Eng. Chem. Res.* **57**, 2165–2177 (2018).
18. da Cunha, S. C. & Resasco, J. Maximizing single-pass conversion does not result in practical readiness for CO2 reduction electrolyzers. *Nat. Commun.* **14**, 5513 (2023).
19. Dinh, C.-T. et al. CO_2 electroreduction to ethylene via hydroxide-mediated copper catalysis at an abrupt interface. *Science* **360**, 783–787 (2018).
20. GarcÃa de Arquer, F. P. et al. CO_2 electrolysis to multicarbon products at activities greater than 1 A cm^{-2}. *Science* **367**, 661–666 (2020).
21. Wang, Y. et al. Catalyst synthesis under CO_2 electroreduction favours faceting and promotes renewable fuels electrosynthesis. *Nat. Catal.* **3**, 98–106 (2020).
22. Li, F. et al. Molecular tuning of CO_2-to-ethylene conversion. *Nature* **577**, 509–513 (2020).
23. Gabardo, C. M. et al. Continuous carbon dioxide electroreduction to concentrated multi-carbon products using a membrane electrode assembly. *Joule* **3**, 2777–2791 (2019).
24. Wu, H. et al. Selective and energy-efficient electrosynthesis of ethylene from CO_2 by tuning the valence of Cu catalysts through aryl diazonium functionalization. *Nat. Energy* **9**, 422–433 (2024).
25. Huang, J. E. et al. CO_2 electrolysis to multicarbon products in strong acid. *Science* **372**, 1074–1078 (2021).
26. Chen, Y. et al. Efficient multicarbon formation in acidic CO_2 reduction via tandem electrocatalysis. *Nat. Nanotechnol.* **19**, 311–318 (2024).
27. Fan, M. et al. Cationic-group-functionalized electrocatalysts enable stable acidic CO_2 electrolysis. *Nat. Catal.* **6**, 763–772 (2023).
28. Zhao, Y. et al. Conversion of CO_2 to multicarbon products in strong acid by controlling the catalyst microenvironment. *Nat. Synth.* **2**, 403–412 (2023).
29. Cao, Y. et al. Surface hydroxide promotes CO_2 electrolysis to ethylene in acidic conditions. *Nat. Commun.* **14**, 2387 (2023).
30. Kim, D. et al. Acid-stable Cu cluster precatalysts enable high energy and carbon efficiency in CO_2 electroreduction. *J. Am. Chem. Soc.* **146**, 27701–27712 (2024).
31. Jouny, M., Luc, W. & Jiao, F. High-rate electroreduction of carbon monoxide to multi-carbon products. *Nat. Catal.* **1**, 748–755 (2018).
32. Ozden, A. et al. Cascade CO_2 electroreduction enables efficient carbonate-free production of ethylene. *Joule* **5**, 706–719 (2021).
33. Ozden, A. et al. Energy- and carbon-efficient CO_2/CO electrolysis to multicarbon products via asymmetric ion migration–adsorption. *Nat. Energy* **8**, 179–190 (2023).
34. Ma, W. et al. Copper lattice tension boosts full-cell CO electrolysis to multi-carbon olefins and oxygenates. *Chem* **9**, 2161–2177 (2023).
35. Li, H. et al. CO electrolysis to multicarbon products over grain boundary-rich Cu nanoparticles in membrane electrode assembly electrolyzers. *Nat. Commun.* **15**, 4603 (2024).
36. Liang, Y. et al. Efficient ethylene electrosynthesis through C–O cleavage promoted by water dissociation. *Nat. Synth.* **3**, 1104–1112 (2024).
37. Miao, R. K. et al. CO electrolysers with 51% energy efficiency towards C_{2+} using porous separators. *Nat. Energy* **10**, 1197–1204 (2025).
38. Li, F. et al. Electrosynthesis of ethylene from syngas. *Nat. Sustain.* https://doi.org/10.1038/s41893-025-01764-w (2026).
39. Zhang, B. et al. Highly electrocatalytic ethylene production from CO_2 on nanodefective Cu nanosheets. *J. Am. Chem. Soc.* **142**, 13606–13613 (2020).
40. Chen, X. et al. Electrochemical CO_2-to-ethylene conversion on polyamine-incorporated Cu electrodes. *Nat. Catal.* **4**, 20–27 (2020).
41. Nam, D. H. et al. Molecular enhancement of heterogeneous CO_2 reduction. *Nat. Mater.* **19**, 266–276 (2020).
42. Cheng, T., Xiao, H. & Goddard, W. A. Full atomistic reaction mechanism with kinetics for CO reduction on Cu(100) from ab initio molecular dynamics free-energy calculations at 298 K. *Proc. Natl Acad. Sci. USA* **114**, 1795–1800 (2017).
43. Wang, X. et al. Efficient electrically powered CO_2-to-ethanol via suppression of deoxygenation. *Nat. Energy* **5**, 478–486 (2020).
44. Peng, H. J., Tang, M. T., Halldin Stenlid, J., Liu, X. & Abild-Pedersen, F. Trends in oxygenate/hydrocarbon selectivity for electrochemical CO_2 reduction to C2 products. *Nat. Commun.* **13**, 1399 (2022).

45. Smith, B. D., Irish, D. E., Kedzierzawski, P. & Augustynski, J. A surface enhanced Roman scattering study of the intermediate and poisoning species formed during the electrochemical reduction of CO_2 on copper. *J. Electrochem. Soc.* **144**, 4288 (1997).
46. Gunathunge, C. M. et al. spectroscopic observation of reversible surface reconstruction of copper electrodes under CO_2 reduction. *J. Phys. Chem. C* **121**, 12337–12344 (2017).
47. Zhan, C. et al. Revealing the CO coverage-driven C-C coupling mechanism for electrochemical CO_2 reduction on Cu_2O nanocubes via *operando* Raman spectroscopy. *ACS Catal.* **11**, 7694–7701 (2021).
48. Bellunato, A. et al. Dynamic tunneling junctions at the atomic intersection of two twisted graphene edges. *Nano Lett.* **18**, 2505–2510 (2018).
49. An, H. et al. Sub-second time-resolved surface-enhanced Raman spectroscopy reveals dynamic CO intermediates during electrochemical CO_2 reduction on copper. *Angew. Chem. Int. Ed.* **60**, 16576–16584 (2021).
50. Carbon intensity of electricity generation. *Our World in Data* https://archive.ourworldindata.org/20251014-145858/grapher/carbon-intensity-electricity.html (2023).
51. Kresse, G. & Hafner, J. Ab initio molecular dynamics for liquid metals. *Phys. Rev. B* **47**, 558–561 (1993).
52. Kresse, G. & Hafner, J. Ab initio molecular-dynamics simulation of the liquid-metal–amorphous-semiconductor transition in germanium. *Phys. Rev. B* **49**, 14251–14269 (1994).
53. Perdew, J. P., Burke, K. & Ernzerhof, M. Generalized gradient approximation made simple. *Phys. Rev. Lett.* **77**, 3865–3868 (1996).
54. Monkhorst, H. J. & Pack, J. D. Special points for Brillouin-zone integrations. *Phys. Rev. B* **13**, 5188–5192 (1976).
55. Montoya, J. H., Shi, C., Chan, K. & NÃ¸rskov, J. K. Theoretical insights into a CO dimerization mechanism in CO_2 electroreduction. *J. Phys. Chem. Lett.* **6**, 2032–2037 (2015).
56. Grimme, S., Antony, J., Ehrlich, S. & Krieg, H. A consistent and accurate ab initio parametrization of density functional dispersion correction (DFT-D) for the 94 elements H-Pu. *J. Chem. Phys.* **132**, 154104 (2010).
57. Zhang, B., Lui, Y. H., Ni, H. & Hu, S. Bimetallic $(Fe_xNi_{1-x})_2P$ nanoarrays as exceptionally efficient electrocatalysts for oxygen evolution in alkaline and neutral media. *Nano Energy* **38**, 553–560 (2017).

Acknowledgements

This work was financially supported by the Ontario Research Foundation: Research Excellence Program, the Natural Sciences and Engineering Research Council (NSERC) of Canada, TotalEnergies SE and the Australian Research Council (project number DE200100477). Synchrotron experiments were performed at SXRMB beamline at the Canadian Light Source (CLS). We acknowledge Q. Xiao, M. Shakouri and A. Paterson for their technical assistance. All DFT computations were performed on the IBM BlueGene/Q supercomputer with support from the Southern Ontario Smart Computing Innovation Platform (SOSCIP) and Niagara supercomputer at the SciNet HPC Consortium. SOSCIP is funded by the Federal Economic Development Agency of Southern Ontario, the Province of Ontario, IBM Canada Ltd, Ontario Centres of Excellence, Mitacs and 15 Ontario academic member institutions. SciNet is funded by the Canada Foundation for Innovation, the Government of Ontario, the Ontario Research Fund—Research Excellence and the University of Toronto. We acknowledge the Ontario Centre for the Characterization of Advanced Materials (OCCAM) for characterization facilities.

Author contributions

E.H.S. and D.S. supervised the project. Y. Chen conceived the idea, designed and conducted the experiments, and wrote the manuscript. P.O. performed the DFT calculations. X.W. contributed to electrochemical experiments and data analysis. R.K.M. conducted the energy cost analysis and life cycle assessment. Y. Chang and X.-Y.L. assisted with DFT calculations. W.N. and R.D. contributed to XAS measurements. A.O., J.E.H., J.Z. and K.X. contributed to data analysis and discussions and manuscript preparation. All authors discussed the results and assisted with manuscript preparation.

Competing interests

There is a US provisional patent application (63/513,432) titled 'Processes and systems for the electrochemical reduction of carbon monoxide and/or carbon dioxide, cathodes and catalysts used in the same' filed by the authors Y. Chen, P.O., E.H.S. and their institutions. The other authors declare no competing interests.

Additional information

Supplementary information The online version contains supplementary material available at https://doi.org/10.1038/s41893-026-01849-0.

Correspondence and requests for materials should be addressed to David Sinton or Edward H. Sargent.

Peer review information *Nature Sustainability* thanks Hailiang Wang and the other, anonymous, reviewer(s) for their contribution to the peer review of this work.

nature portfolio

Corresponding author(s): Edward H. Sargent

Last updated by author(s): Apr 3, 2026

Reporting Summary

Nature Portfolio wishes to improve the reproducibility of the work that we publish. This form provides structure for consistency and transparency in reporting. For further information on Nature Portfolio policies, see our Editorial Policies and the Editorial Policy Checklist.

Statistics

For all statistical analyses, confirm that the following items are present in the figure legend, table legend, main text, or Methods section.

n/a	Confirmed	
☐	☒	The exact sample size (*n*) for each experimental group/condition, given as a discrete number and unit of measurement
☐	☒	A statement on whether measurements were taken from distinct samples or whether the same sample was measured repeatedly
☒	☐	The statistical test(s) used AND whether they are one- or two-sided *Only common tests should be described solely by name; describe more complex techniques in the Methods section.*
☒	☐	A description of all covariates tested
☒	☐	A description of any assumptions or corrections, such as tests of normality and adjustment for multiple comparisons
☐	☒	A full description of the statistical parameters including central tendency (e.g. means) or other basic estimates (e.g. regression coefficient) AND variation (e.g. standard deviation) or associated estimates of uncertainty (e.g. confidence intervals)
☒	☐	For null hypothesis testing, the test statistic (e.g. *F*, *t*, *r*) with confidence intervals, effect sizes, degrees of freedom and *P* value noted *Give P values as exact values whenever suitable.*
☒	☐	For Bayesian analysis, information on the choice of priors and Markov chain Monte Carlo settings
☒	☐	For hierarchical and complex designs, identification of the appropriate level for tests and full reporting of outcomes
☒	☐	Estimates of effect sizes (e.g. Cohen's *d*, Pearson's *r*), indicating how they were calculated

Our web collection on statistics for biologists contains articles on many of the points above.

Software and code

Policy information about availability of computer code

Data collection	Does not apply
Data analysis	Does not apply

For manuscripts utilizing custom algorithms or software that are central to the research but not yet described in published literature, software must be made available to editors and reviewers. We strongly encourage code deposition in a community repository (e.g. GitHub). See the Nature Portfolio guidelines for submitting code & software for further information.

Data

Policy information about availability of data

All manuscripts must include a data availability statement. This statement should provide the following information, where applicable:

- Accession codes, unique identifiers, or web links for publicly available datasets
- A description of any restrictions on data availability
- For clinical datasets or third party data, please ensure that the statement adheres to our policy

The data supporting this study are available within the paper and the Supplementary Information. The source dataset is provided.

Research involving human participants, their data, or biological material

Policy information about studies with human participants or human data. See also policy information about sex, gender (identity/presentation), and sexual orientation and race, ethnicity and racism.

Reporting on sex and gender	Dose not apply
Reporting on race, ethnicity, or other socially relevant groupings	Dose not apply
Population characteristics	Dose not apply
Recruitment	Dose not apply
Ethics oversight	Dose not apply

Note that full information on the approval of the study protocol must also be provided in the manuscript.

Field-specific reporting

Please select the one below that is the best fit for your research. If you are not sure, read the appropriate sections before making your selection.

☐ Life sciences ☐ Behavioural & social sciences ☒ Ecological, evolutionary & environmental sciences

For a reference copy of the document with all sections, see nature.com/documents/nr-reporting-summary-flat.pdf

Ecological, evolutionary & environmental sciences study design

All studies must disclose on these points even when the disclosure is negative.

Study description	This study investigates systems and catalysts for electrified ethylene synthesis that minimize the combined energy cost of carbon electrolysis and tailgas separation. Key performance metrics include Faradaic efficiency (FE), energy efficiency (EE), SPCE, product concentration in the outlet stream and energy cost for ethylene production.
Research sample	The research sample consists of synthesized Cu nanosheet catalysts modified with inorganic heteroatom-doped carbon overlayers (N-C, P-C, and N,P-C). The Cu nanosheets serve as the baseline catalyst, and the modified samples are intended to represent a class of robust, inorganic-modified electrocatalysts for CO-to-ethylene conversion. The study does not involve biological organisms or ecological populations; it focuses on material synthesis, electrochemical characterization, and system-level performance evaluation.
Sampling strategy	No formal statistical sample-size calculation was performed a priori. Sample sizes (number of independent electrode replicates per condition) were chosen based on established practices in electrocatalysis and materials science, where triplicate measurements are commonly used to assess reproducibility and account for experimental variability in electrode fabrication and electrochemical testing. This approach is sufficient to determine significant trends in catalytic performance and ensure reliability of the reported data.
Data collection	Electrochemical data were collected using a potentiostat in a custom built zero gap MEA electrolyzer. Gaseous products were analyzed using gas chromatography (GC). The liquid products were measured by 1H NMR spectroscopy (600 MHz Agilent DD2 NMR Spectrometer) with dimethyl sulfoxide (DMSO) as the reference standard and deuterium oxide (D2O) as the lock solvent. Catalyst characterization was performed using scanning electron microscopy (SEM), energy dispersive X ray spectroscopy (EDS), X ray photoelectron spectroscopy (XPS), X ray absorption spectroscopy (XAS), and operando Raman spectroscopy. All data were recorded by trained researchers in the laboratory following standardized protocols.
Timing and spatial scale	Data collection was conducted over a period of near four years, from Jan. 2022 to Dec. 2025. Electrochemical experiments were performed during this period. The spatial scale of the study is confined to research labs. No field based or geographically distributed sampling was involved.
Data exclusions	No data were excluded from the analyses. All collected measurements from independent replicates are included in the results and supplementary information.
Reproducibility	The key findings—including the enhancement in ethylene EE and SPCE, the high product outlet concentration with N,P-C/Cu, and the trade-off behavior on pristine Cu—were each confirmed through at least three independent experimental replicates.
Randomization	Randomization is not applicable to this study. Each catalyst group was tested under identical experimental setups to ensure direct comparability.
Blinding	Blinding was not relevant to this study because the data acquisition and analysis processes in materials science and electrocatalysis are objective, instrument-based, and operator-independent. Electrochemical measurements (e.g., current, potential) were recorded automatically by a potentiostat, and product quantification was performed via gas chromatography using calibrated standards. Material characterization (SEM, XPS, Raman, etc.) was conducted with well-established instrumental protocols, and data

interpretation relied on quantitative spectral analysis and reference databases. Since all measurements were based on instrumental outputs and standardized analytical methods, there was no subjective judgment involved that would necessitate blinding of the researchers during data collection or analysis.

Did the study involve field work? ☐ Yes ☒ No

Reporting for specific materials, systems and methods

We require information from authors about some types of materials, experimental systems and methods used in many studies. Here, indicate whether each material, system or method listed is relevant to your study. If you are not sure if a list item applies to your research, read the appropriate section before selecting a response.

Materials & experimental systems

n/a	Involved in the study
☒	☐ Antibodies
☒	☐ Eukaryotic cell lines
☒	☐ Palaeontology and archaeology
☒	☐ Animals and other organisms
☒	☐ Clinical data
☒	☐ Dual use research of concern
☒	☐ Plants

Methods

n/a	Involved in the study
☒	☐ ChIP-seq
☒	☐ Flow cytometry
☒	☐ MRI-based neuroimaging

Plants

Seed stocks: Does not apply

Novel plant genotypes: Does not apply

Authentication: Does not apply